ACS APPLIED MATERIALS & INTERFACES

RESEARCH ARTICLE

www.acsami.org

One-Step Hydrothermal Synthesis of Mesoporous Anatase TiO_2 Microsphere and Interfacial Control for Enhanced Lithium Storage Performance

Kyung-Ho Lee and Seung-Wan Song*

Department of Fine Chemical Engineering & Applied Chemistry, Chungnam National University, Daejeon, 305-764, South Korea

Supporting Information

ABSTRACT:

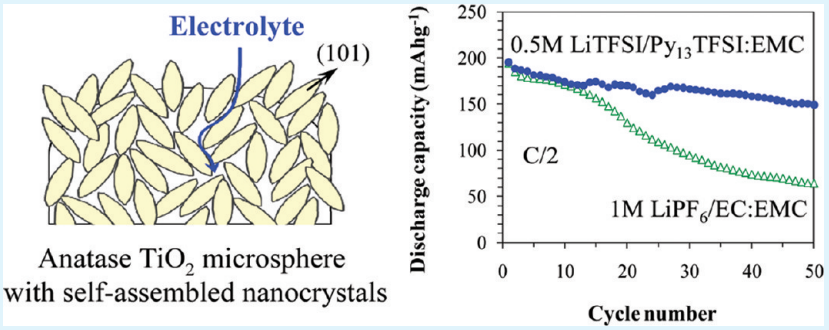

Mesoporous TiO_2 anatase microspheres consisting of self-assembled nanocrystals have been synthesized by a one-step hydrothermal method at 120 °C using titanium-peroxo complex, without a post-calcination process. Transmission and scanning electron microscopic imaging reveal that diamond-shaped nanocrystals as primary particles, which are 20 nm in average width and 50 nm in length and oriented with (101) plane of anatase phase, are aggregated to form a secondary microsphere particle with 0.5−1 μm in diameter. BET analysis data show that the TiO_2 anatase particles possess significantly large surface area of 254 $m^2\ g^{-1}$ with the pore size of ∼14 nm. Mesoporous TiO_2 anatase anode shows an enhanced lithium storage performance in pyrrolidinium-based ionic liquid electrolyte diluted with ethyl methyl carbonate, delivering 195 - 150 $mAhg^{-1}$ at the C/2 rate with 77 % capacity retention and 98−99 % Coulombic efficiencies over 50 cycles despite the absence of surface carbon-coating. AC impedance analysis results reveal that the formation of a stable solid electrolyte interphase (SEI) layer in diluted ionic liquid electrolyte induces the enhanced cycling performance. Control of electrode-electrolyte interfacial compatibility enables the enhancement of cycling performance and the preservation of microstructure. The data contribute to provide cost-efficient synthetic method for the TiO_2 and the interfacial control aspect of performance control for safer batteries.

KEYWORDS: lithium-ion batteries, one-step hydrothermal synthesis, anatase TiO_2, mesoporous microsphere, ionic liquid-based electrolyte, SEI layer, interfacial control

1. INTRODUCTION

Titanium dioxide (TiO_2) materials with large surface area and tunable pore size are appealing to energy applications, due to their high reactivity and prompt response.[1,2] In lithium-ion batteries, the TiO_2 is an attractive alternative anode material to graphite because of its sufficiently high enough operating voltage ∼1.75 V vs. Li/Li^+ as well as abundance in resources for safer and cost-efficient batteries. Nanostructuring[3−5] and tuning the particle size and porosity[6−9] of the TiO_2, and carbon-coating on the surface of the TiO_2 particle[10−13] enabled the formation of porous nanomaterials with improved electrochemical activity. They however tend to result in low volumetric energy density and particle morphology change (e.g., aggregation) with repeated charge (lithium intercalation) and discharge (lithium deintercalation) cycling, which affect the electrochemical cycling performance. The use of nanomaterials is subjected to the difficulties in handling and additional cost for the electrode fabrication process.[13] Micro- or submicrometer scaled materials are often preferred in the large-scale production but they can result in either limited reaction kinetics, inhomogeneous current distribution from surface to bulk, or inferior interfacial contact with electrolyte. The design of particle shape (a micrometer secondary particle composed of primary nanocrystals) would be desirable for having large surface area but robust structure and morphology. Particles can then withstand long-term cycling and the electrode fabrication process can be efficient.

A variety of chemical synthetic methods have been reported for preparing the TiO_2 nanomaterials ranged from sol−gel,[8]

Received: July 4, 2011
Accepted: August 18, 2011
Published: August 18, 2011

hydrolysis, or precipitation[6,7,9,14] to hydrothermal[2,4,10,12] method, mostly in a manner that uses surfactant or template for the growth of anisotropic nanocrystals. The relationship of structure−morphology−function has been extensively studied.[2,14,15] Phase selection (rutile, anatase, or brookite), particle shape and size, as well as crystal orientation with specific lattice plane and porosity were controllable depending on synthetic conditions.[1,14,16−18] For the synthesis of the TiO_2, alkoxides,[4,6−10,12,13] chloride,[17] or sulfate[14] reactants have often been used as the source of titanium. They are, however, difficult to handle in the air and in aqueous solution because of high reactivity to moisture and fast hydrolysis rate, respectively. Recently, the TiO_2 itself was used as a reactant for hydrothermal synthesis in alkaline condition.[3,18] The reaction procedure then often included either strong acidic or alkaline solution. Moreover, most synthetic methods include the post-calcination of precursor at temperatures over 300 °C for promoted TiO_2 crystallization and the removal of residual organics. The development of simpler synthetic procedure including low temperature and neutral reaction solution without post-calcination is highly demanded.

The thermal decomposition of electrolyte and the solid electrolyte interphase (SEI) layer often reduce safety and durability of batteries.[19] Even though the SEI layer has been reported not to form on the high voltage titanium oxides operated over 1.0 V vs. Li/Li^+, it was clarified on the $Li_4Ti_5O_{12}$ that the SEI layer forms and the SEI composition plays a crucial role in controlling cycling performance.[20] The interfacial control of the SEI formation and composition is believed to be a promising approach to enhance the cycling performance of battery electrodes.[21,22] Recently room temperature ionic liquid electrolytes have received a particular attention as an alternative electrolyte to conventional carbonate-based electrolyte due to their non−flammability, and high electrochemical and thermal stabilities[23,24] for safer batteries. Limited work has been performed to evaluate the cathodic stability of room temperature ionic liquid electrolyte. Oh et al.[25] described that the imidazolium-based ionic liquid electrolyte on the TiO_2 bronze is cathodically unstable, whereas the pyrrolidinium- and piperidinium-based ones are stable. Nevertheless, overcoming a relatively high viscosity and low ionic conductivity of ionic liquid is needed in the practical use of batteries. Dilution of the ionic liquid electrolyte with carbonate−based organic solvent (e.g., ethyl methyl carbonate (EMC)) can lower viscosity but increase the ionic conductivity.[26]

In this work, we report a simple one-step hydrothermal synthesis of crystalline and mesoporous TiO_2 anatase microspheres that consist of self-assembled primary nanocrystals, using titanium-peroxo complex without post-calcination. We utilize the benefit of hydrothermal particle aggregation (Ostwald ripening) to promote the growth of secondary particles, rather than molecular addition to the growth of anisotropic primary particles. The mesopores present between diamond-shaped nanocrystals, which are rooted on a microsphere, permit facile interfacial contact with the electrolyte and easy penetration of Li^+ ions while maintaining the morphology of microspheres with electrochemical cycling. The electrochemical performance and stability, together with interfacial compatibility of our meroporous TiO_2 anatase anode in the lithium cells with ionic liquid-based electrolytes of 1 M $LiTFSI/Py_{13}TFSI$ and 0.5 M $LiTFSI/Py_{13}TFSI$:EMC with 1:1 volume ratio are demonstrated.

2. EXPERIMENTAL SECTION: MATERIALS AND METHODS

Synthesis and Characterization of Anatase TiO_2. The Ti powder (Aldrich, 99.7%) was dissolved in hydrogen peroxide (Samchun chemicals, 34.5 wt %) first. Then nitric acid (Samchun chemicals, 60.0 wt %) was added to the red orange-colored solution of titanium-peroxo complex. The molar ratio for $Ti:H_2O_2:HNO_3$ was 0.05:94:6.2. The mixed solution in a plastic (Nalgene) bottle was placed in the convection oven at 65 °C for 1 day for a complete dissolution. The resulting transparent solution, 2-propanol (Aldrich, > 99.5%), and distilled water were mixed in 2:1:1 volume ratio and stirred. The pH of the solution was near 2. NH_4OH (Samchun chemicals, 28.0−30.0 wt %) was added to the solution to adjust the pH to 7, resulting in the color change of the solution to pale yellow. The 63.3 mL of neutralized yellow solution was taken to the Teflon-lined autoclave in 100 mL volume and the autoclave was tightly closed. The hydrothermal reaction was carried out at 120 °C for 6 h. After the hydrothermal synthesis, the pH of remained solution was 10. The produced solid precipitates were separated from the residual solution by centrifugation at 3200 rpm and washed with distilled water several times until the pH reaches 7. The obtained precipitates were dried in the convection oven at 65 °C for 1 day. The color of the final solid powders was light beige.

Particle morphology was examined using field-emission scanning electron microscopy (FESEM, Hitachi S-4800) at 15 kV. The nanostructure of synthesized materials was analyzed using high-resolution transmission electron microscopy (HRTEM, JEOL JEM-2100F (HR)) at 200 kV. The TEM specimens were prepared by dispersing the synthesized powders in ethanol by sonication and placing a drop of the dispersion on carbon-coated copper grids followed by evaporating ethanol. The crystal structure of hydrothermally synthesized materials was determined by powder X-ray diffraction using an X-ray diffractometer (Bruker AXS/D8 DISCOVER), which was measured from 15 to 65° 2θ with the scan rate of 1°/min at 0.02° step. The pore structure of the synthesized material was characterized by N_2 adsorption at −196 °C using an adsorption apparatus (BELSORP-max). The surface area was determined from Brunauer-Emmett-Teller (BET) equation, and pore size distribution from the isotherm adsorption branches based on the Barrett−Joyner−Halenda (BJH) model.

Electrode Preparation and Electrochemical Characterization. The TiO_2 electrode was fabricated by coating a slurry, which was composed of 75 wt % TiO_2 active material, 10 wt % carbon black, and 15 wt % polyvinylidene fluoride (PVdF, Aldrich) binder in N-methyl-2-pyrrolidone (NMP, Aldrich) solvent, on a copper foil to approximately 60 μm in thickness. The coated slurry was dried in a vacuum oven at 110 °C for 12 h and pressed using a roll press with a pressure of 30 kg cm^{-1} at room temperature. The prepared electrodes were stored in the Ar-filled glove box (MOTek) with water and oxygen contents of 1 ppm.

The electrochemical behavior of the TiO_2 electrode was evaluated using lithium cells with the TiO_2 electrode as working electrode, and lithium reference and counter electrodes in 1 M $LiPF_6$/ethylene carbonate (EC):ethyl methyl carbonate (EMC) (3:7 volume ratio) (Techno Semichem), 1M lithium bis(trifluoromethylsulfonyl)imide (LiTFSI)/1−methyl−1−propylpyrrolidinium bis(trifluoromethylsulfonyl)imide ($Py_{13}TFSI$) and diluted ionic liquid electrolyte containing 50 vol % of 1 M $LiTFSI/Py_{13}TFSI$ and 50 vol % of EMC, which results in the reduced concentration of lithium salt to 0.5 M, with separator (Celgard 2400). Prior to the preparation of ionic liquid electrolyte, the $Py_{13}TFSI$ (> 99%, Citri) and LiTFSI (99.95 %, Aldrich) were dried in the vacuum oven at 110 °C for 48 h for the removal of water. Galvanostatic charge (lithium intercalation)−discharge (lithium deintercalation) cycling was conducted in the voltage region of 1.0−2.5 V vs. Li/Li^+ at the $C/2$ rate using a multichannel galvanostat (Won-A Tech). Note that the 1C rate refers to the current density of 335 mA g^{-1} applied to the cell for charging or discharging to reach the theoretical capacity of 335 $mAhg^{-1}$ in 1 h, which corresponds to the 1 mol of lithium intercalation and deintercalation to/from the anatase TiO_2. The AC impedance measurement was conducted using an impedance analyzer (VSP SP-150) over

the frequency range of 100 kHz to 5 mHz with an amplitude of 10 mV. Impedance spectra were collected at the fully charged (1.0 V) and discharged (2.5 V) states, respectively. Before measurement, lithium cells were left to relax at open circuit until they reached the equilibrium.

Changes in particle morphology of the TiO_2 electrode with cycling were examined using ex situ field-emission SEM. Cycled electrodes were separated from the lithium cells and washed with dimethyl carbonate (DMC) for 20s for the removal of residual electrolyte followed by drying in the Ar-filled glove box at room temperature. Electrolyte preparation, cell assembly/disassembly, and electrochemical testing were carried out in the glove box.

3. RESULTS AND DISCUSSION

Synthesis and Structural characterizations. The dissolution of the Ti powder in hydrogen peroxide, a strong oxidizing agent, results in the oxidation of the Ti to the Ti^{4+}. This forms red orange-colored dinuclear titanium-peroxo cation $[Ti^{4+}{}_2O(O_2)_2]^{2+}$ in formula 1 and complex $[Ti^{4+}{}_2O(O_2)_2](OH)_2$, where the Ti^{4+} cation is coordinated by peroxide (O_2^-) and hydroxide (OH^-) from water.[17,27−29] Upon the addition of 2-propanol and water to the titanium-peroxy complex followed by the adjustment of pH to 7 with NH_4OH, the complex is further coordinated by hydroxide and/or propanoxy anion as expressed in formulae 2 and 3, resulting in color change to pale yellow. They can condense to polynuclear species and supersaturate under hydrothermal condition. Finally, the homogeneous nucleation to the TiO_2 occurs followed by crystal growth,

$$2Ti + 2H_2O_2 \rightarrow [Ti_2^{4+}O(O_2)_2]^{2+} + 2H^+ + 4e^- \quad (1)$$

$$[Ti_2^{4+}O(O_2)_2]^{2+} + 2H_2O \rightarrow [Ti_2^{4+}O(O_2)_2](OH)_2$$

$$+ 2H^+ \xrightarrow{\text{hydrothermal}} 2TiO_2 + 2OH^- + H_2O \quad (2)$$

$$[Ti_2^{4+}O(O_2)_2]^{2+} + ROH \rightarrow [Ti_2^{4+}O(O_2)_2](OR)_2$$

$$+ 2H^+ \xrightarrow{\text{hydrothermal}} 2TiO_2 + 2OR^- + H_2O \quad (3)$$

where ROH is 2-propanol. Because no surfactant or template for directing the crystal growth was used in this work, the crystal growth of anatase TiO_2 is estimated to readily undergo along the most thermodynamically stable (101) surface.[30] The presence of hydroxide anions in 2 after hydrothermal reaction is consistent with an increase in the residual solution pH.

The morphology of the as-prepared TiO_2 was characterized by SEM and TEM, as shown in Figure 1. SEM image in Figure 1a reveals that the one-step hydrothermal reaction results in the formation of microsphere particles with the diameter of 0.5−1 μm and rough surface. High-magnification image in Figure 1b shows that a microsphere consists of self-assembled, diamond-shaped nanocrystals with an average of 20 nm in width and an average of 50 nm in length. This indicates that the hydrothermal reaction leads to the aggregation (Ostwald ripening) of individual nanocrystals to grow to a secondary particle of microsphere, rather than molecular addition to the growth of anisotropic primary particle. Figure 1c shows the TEM image for the side view of a single TiO_2 microsphere, ensuring that a microsphere is composed of self-assembled, diamond-shaped TiO_2 nanocrystals. A high resolution TEM image focused on a single diamond-shaped nanocrystal in Figure 1d reveals just one lattice fringe with the

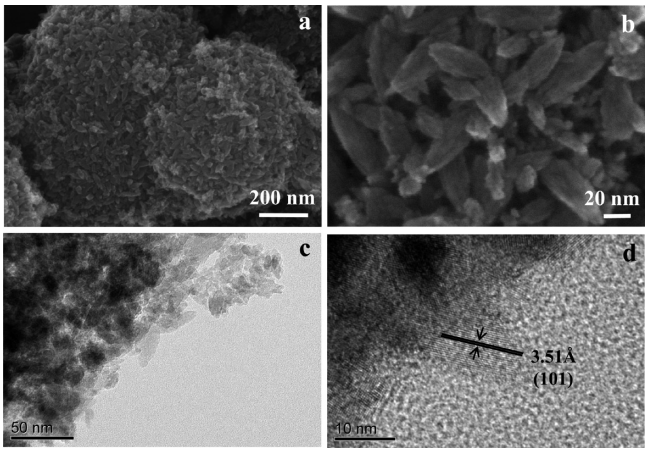

Figure 1. (a, b) SEM and (c, d) HRTEM images for the as-prepared TiO_2.

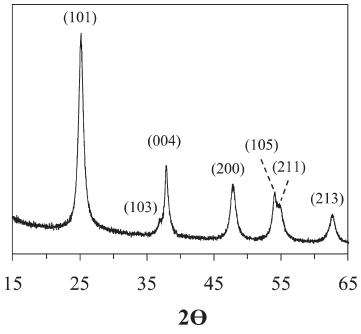

Figure 2. X-ray diffraction pattern of the as-prepared TiO_2.

3.51 Å in width. This corresponds to the (101) lattice plane of the anatase TiO_2 phase. Diamond-shaped crystals are oriented with the (101) plane, consistent with the line texture which appeared on the individual nanocrystals in Figure 1b. Note that the (101) surface of anatase TiO_2 is known to be the most thermodynamically stable.[30] Relevant literature showed that the equilibrium shape of anatase TiO_2 could be drawn as a truncated bipyramid, exposing eight equivalent (101) facets on the side surface and two equivalent (001) facets on the top and bottom facets.[30,31] The lengthened diamond shape of our anatase TiO_2 nanocrystal is due to dominant crystal growth with the (101) surface.

Powder X-ray diffraction pattern in Figure 2 exhibits that all reflections correspond to the TiO_2 crystallized in the anatase phase with tetragonal ($I41/amd$) structure (JCPDS 21-1272). Cell parameters are determined to be $a = b = 3.8053$ Å and $c = 9.4776$ Å. Figure 3a shows the N_2 adsorption−desorption isotherm of the as-prepared TiO_2 powders with a clear condensation step at relative pressures and a hysteresis loop. The isotherm is identified as type IV, which is characteristic of mesoporous materials.[32] The average pore size in Figure 3b is 14 nm and the pore volume is 0.35 $cm^3\ g^{-1}$. The surface area determined by the Brunauer−Emmett−Teller (BET) measurement is 254 $m^2\ g^{-1}$. Such large surface area with the presence of mesopores should provide facile interfacial contact with electrolyte and promoted transport kinetics of Li^+ ions,[33,34] as depicted in a cross-sectional schematic in Figure 3c.

Electrochemical Characterization and Interfacial Compatibility. Figure 4 shows charge and discharge voltage profiles of

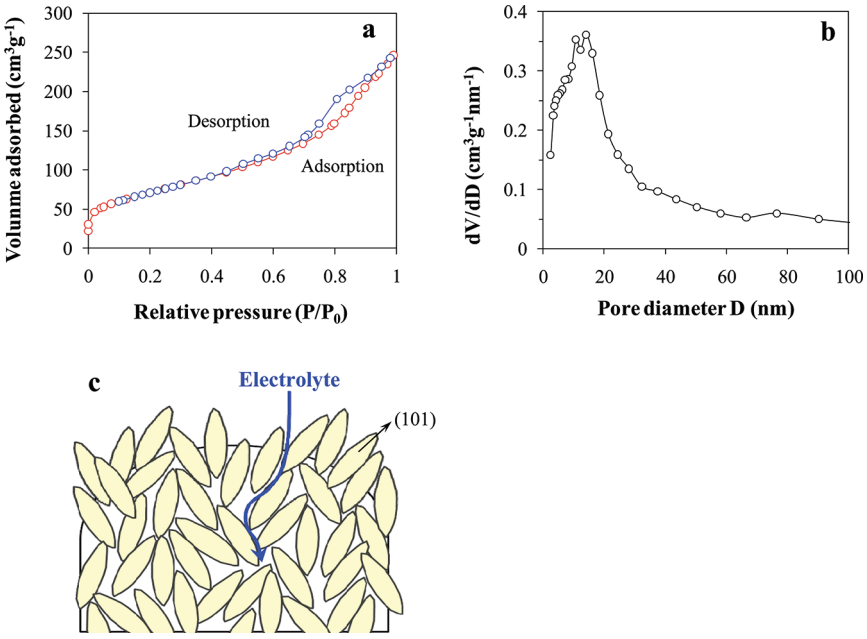

Figure 3. (a) N_2 adsorption−desorption isotherm and (b) pore size distribution of the as-prepared TiO_2, and (c) schematic of a mesoporous microsphere with self-assembled diamond-shaped anatase TiO_2 nanocrystals.

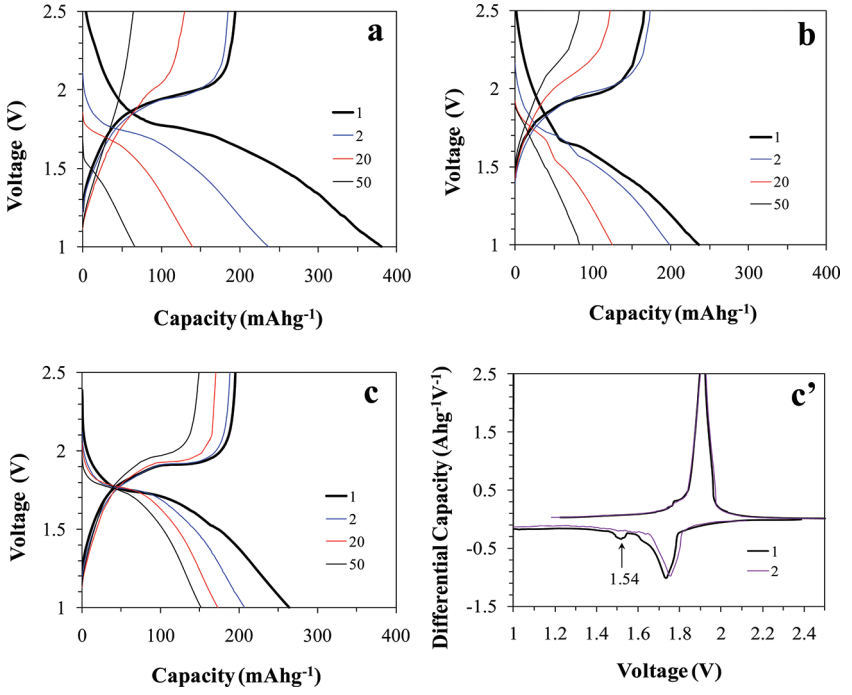

Figure 4. Voltage profiles for lithium cells with anatase TiO_2 electrode in (a) 1 M $LiPF_6$/EC:EMC, (b) 1 M LiTFSI/Py_{13}TFSI, and (c) 0.5 M LiTFSI/Py_{13}TFSI:EMC (vol 1:1) at different cycle number, and (c′) its differential capacity plot at the first and second cycles.

lithium cells with the anatase TiO_2 electrodes in the voltage region of 1.0−2.5 V vs. Li/Li^+ at the $C/2$ rate ($1C = 335$ mA g^{-1}) in different electrolytes. Charge curves exhibit in common a plateau near 1.75 V vs. Li/Li^+, associated with the reduction of Ti^{4+} to Ti^{3+} by lithium intercalation ($Li^+ + TiO_2 \rightarrow Li_xTiO_2$) and the coexistence of Li_xTiO_2 in tetragonal anatase structure ($I41/amd$) and new phase in orthorhombic structure ($Imma$) solid solution.[35,36] In the reverse process, a discharge plateau at 1.90 V is due to the lithium deintercalation from the Li_xTiO_2 regenerating the TiO_2.

In the conventional electrolyte of 1 M $LiPF_6$/EC:EMC, in Figure 4a, initial charge capacity is 380 mA h g^{-1}, which exceeds the theoretical value (335 mA h g^{-1}). An extra charge capacity might come from a reductive electrolyte decomposition that forms surface species. Mesoporous TiO_2 anatase with enlarged active surface area can be subjected to interfacial reaction with

electrolyte. It is surprising that the liquid electrolyte of $LiPF_6$/EC:EMC is reduced at such a high voltage region. The EC and EMC are reported to be stable until ~1.3 V vs. Li/Li^+,[19] whereas the $LiPF_6$ is reducible below 2.0 V vs. Li/Li^+,[37] all of which were measured on an inert electrode (e.g., Au). Catalytic electron transfer from the Li_xTiO_2 to electrolyte component seems to occur during lithium intercalation on the initial charge. In addition, the presence of a trace of water in the electrolyte is known to result in the formation of PF_5; $LiPF_6 + H_2O \rightarrow PF_5 + LiF$, $PF_5 + H_2O \rightarrow HF + PF_3O$.[38]

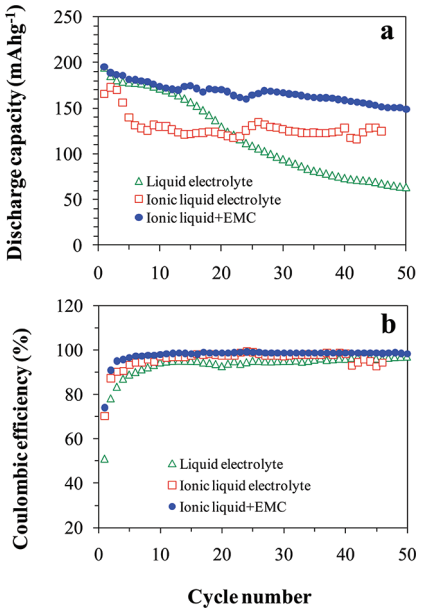

Figure 5. Plots of (a) discharge capacity and (b) Coulombic efficiency as a function of cycle number at the C/2 rate in different electrolytes.

The PF_5 and PF_3O, which are strong Lewis acids, can react with the TiO_2 electrode, forming surface species that can be further reduced electrochemically. The formation of insulating LiF will deleteriously affects the cycling ability. Subsequent discharge capacity is 194 mA h g^{-1}, which gives a low initial Coulombic efficiency of 51 %. Electrolyte reduction together with some lithium ions remained irreversibly as the Li_xTiO_2 might contribute to this large irreversible initial capacity loss. Panels a and b in Figure 5 compare the cycling ability of the TiO_2 electrode at the C/2 in different electrolytes. In the conventional electrolyte, the discharge capacity continuously decreases from 194 to 64 mA h g^{-1} with poor capacity retention of 33% and Coulombic efficiency 80−95% during 50 cycles.

In the ionic liquid electrolyte of 1 M LiTFSI/Py_{13}TFSI, in Figure 4b, the TiO_2 electrode shows the initial charge and discharge capacities of 234 and 166 mA h g^{-1}, respectively, with somewhat improved initial efficiency of 71%. However, the discharge capacity gradually fades with cycling resulting in capacity retention of 75% and efficiencies 90−97 % as seen in panels a and b in Figure 5. This is probably due to the high viscosity of ~63 cP and low ionic conductivity of ~1.4 mS cm^{-1} of the Py_{13}TESI,[23] compared to carbonate-based organic solvents (e.g., ~1.3 cP and 9.4 mS cm^{-1} for EC:EMC (1:1 volume ratio)).[19,26]

Dilution of viscous ionic liquid electrolyte enables to improve the reversibility in cycling. Figure 4c shows voltage profile of lithium cell with the TiO_2 electrode in the diluted ionic liquid electrolyte of 0.5 M LiTFSI/Py_{13}TFSI:EMC. Initial cycling delivers charge and discharge capacities of 264 and 195 mA h g^{-1}, respectively, with a bit improved initial Coulombic efficiency of 74%. The EMC reduction is traceable in the differential capacity plot shown in Figure 4c′. A tiny cathodic peak at 1.54 V is observed in the first charge curve but disappeared in the second cycle. This is attributed to the reductive decomposition of the EMC forming the SEI layer. Significantly small capacity relative to that for Li^+

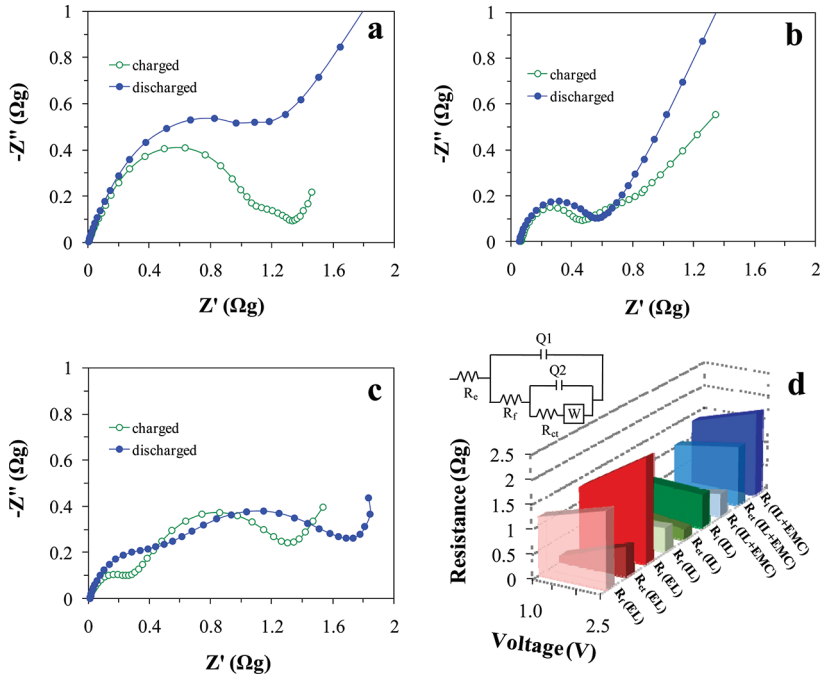

Figure 6. AC impedance spectra for the TiO_2 electrode in (a) 1 M $LiPF_6$/EC:EMC (EL), (b) 1 M LiTFSI/Py_{13}TFSI (IL), (c) 0.5 M LiTFSI/Py_{13}TFSI:EMC (IL+EMC), collected at the fully charged (1.0 V) and discharged (2.5 V) states, and (d) changes in the interfacial resistances determined by fitting the spectra using the equivalent circuit model.

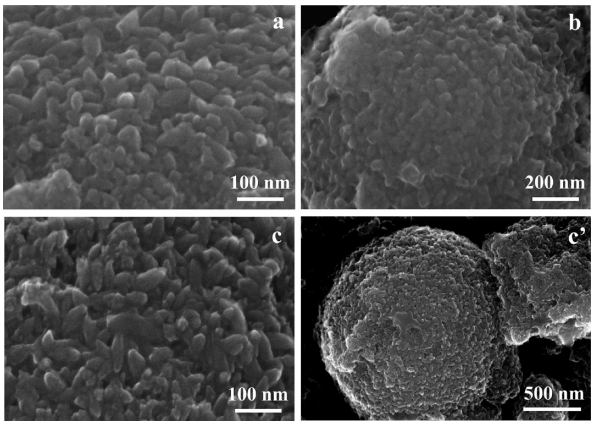

Figure 7. SEM images for the TiO_2 electrode after cycling at the $C/2$ rate in (a) 1 M $LiPF_6$/EC:EMC, (b) 1 M LiTFSI/Py_{13}TFSI, and (c, c′) 0.5 M LiTFSI/Py_{13}TFSI:EMC (vol 1:1).

intercalation and deintercalation reflects the SEI layer to be thin or in a low concentration level. The presence of the EMC appears to provide the effective formation of a stable SEI layer in the early stage of cycling and a facile Li^+ transportation by reducing the viscosity of ionic liquid. In Figure 5a, the TiO_2 electrode in diluted ionic liquid electrolyte delivers discharge capacities of 195−150 mA h g^{-1} with 77 % capacity retention over 50 cycles. Coulombic efficiencies are close to 98−99 % as shown in Figure 5b. The improvement of initial Coulombic efficiency and capacity retention in diluted ionic liquid electrolyte, despite higher viscosity and lower ionic conductivity than conventional electrolyte, reveal that a stable SEI layer forms, which protects the TiO_2 electrode from further electrolyte decomposition.

The initial interfacial behavior of the TiO_2 electrode depending on electrolyte was examined using AC impedance spectroscopy. Impedance spectra were collected at fully charged and discharged states, respectively. As shown in Figure 6, all spectra consist of semicircles in a high to intermediate frequency range associated with overall interfacial resistance (R_i), which includes the resistance of the SEI layer (R_f) and charge transfer resistance (R_{ct}), respectively.[18,39−41] Also shown is a straight slopping line in a low frequency range, attributed to the Warburg diffusion of Li^+ ions to the TiO_2 electrode. High frequency intercept of the real axis (Z') after initial cycle, corresponding to the bulk resistance of the electrolyte, is larger in ionic liquid electrolyte (0.06 Ω) in Figure 6b than other electrolytes (< 0.01 Ω), because of the viscosity of ionic liquid. The dependence of interfacial resistances on charged and discharged states and electrolyte are summarized in Figure 6d. Resistances were determined by fitting the spectra using the equivalent circuit model.

It is evident that in all electrolytes, the semicircles tend to expand, i.e., the R_i tends to increase, with initial charge and discharge, in particular, in conventional electrolyte (Figure 6a,d). It appears that a resistive surface layer forms and thickens by continuous electrolyte decomposition regardless of charge or discharge. Thickened surface layer can hinder or block the Li^+ transport, leading to inferior cycling ability as observed in Figures 4 and 5. On the contrary, the changes in the R_i are relatively smaller in ionic liquid-based electrolytes as shown in Figures 6b−d. This is related to the improved initial Coulombic efficiencies in Figures 4 and 5. Remarkably smaller R_i value in ionic liquid electrolyte than in other electrolytes and its little change indicate that interfacial reaction is not the cause for inferior cycling ability in Figures 4 and 5. The high viscosity probably together with low ionic conductivity of ionic liquid is thought to be the barrier for charge and discharge processes.

In dilute ionic liquid electrolyte (Figure 6c,d), the absolute value of the R_i is larger than that of ionic liquid electrolyte due to the resistive surface layer produced by the EMC decomposition as discussed above. However, a slight change in the R_i upon initial charge and discharge is an indication for the formation of a stable SEI layer, which might suppress irreversible interfacial reactions in the next cycles. The enhanced cycling ability of the TiO_2 electrode in diluted ionic liquid electrolyte in Figures 4 and 5 is believed to be due to the formation of a stable SEI layer during initial cycling and reduced viscosity.

Morphology change due to cycling at the $C/2$ depending on the type of electrolyte was monitored using ex situ SEM, as compared in Figure 7. The nanocrystals in the conventional electrolyte in Figure 7a exhibit volume expansion and tend to be aggregated with cycling. Morphology change is even severe in the ionic liquid electrolyte only (Figure 7b), and diamond-shaped individual nanocrystals are no longer observable after cycling. The drastic morphology change should be associated with irreversible reaction with lithium and surface layer formation by interfacial reactions, as observed in Figures 4 and 5. In diluted ionic liquid electrolyte in Figure 7c-d, the morphology of not only microspheres but also diamond-shaped nanocrystals remains almost unchanged even after cycling despite a slight volume expansion. The surface of nanocrystals becomes smoother and the pores present between nanocrystals are still visible but smaller than the pristine TiO_2. The maintained particle morphology should be related to an enhanced cycling performance in Figures 4 and 5.

4. CONCLUSIONS

The anatase TiO_2 anode material has been synthesized via facile hydrothermal method using 120 °C aqueous titanium-peroxo complex solution without post-calcination. The TiO_2 microspheres consist of self-assembled nanocrystals that are diamond-shaped and oriented with the (101) plane, which provides a large surface area of 254 m^2 g^{-1} and mesoporosity with 14 nm of average pore size. Crystal growth to nanocrystals as primary particles followed by the growth to a secondary particle appears to be favored under the present synthetic condition. The mesopores present between nanocrystals that are rooted on a microsphere permit easy penetration of Li^+ ions from electrolyte while maintaining the microstructure of microspheres. Synthesized anatase TiO_2 is interfacially compatible the most with diluted ionic liquid electrolyte, resulting in the formation of a stable SEI layer and enhanced lithium storage performance, despite the absence of surface carbon coating on the insulating TiO_2. Particle morphology is best maintained after cycling in the diluted ionic liquid electrolyte, whereas they tend to be aggregated in other electrolytes, which is related to charge−discharge cycling performance.

■ ASSOCIATED CONTENT

Supporting Information. Raman spectrum of mesoporous TiO_2 anatase. This material is available free of charge via the Internet at http://pubs.acs.org.

■ AUTHOR INFORMATION

Corresponding Author

*Phone: +82-42-821-7008. Fax: +82-42-822-6637. E-mail: swsong@cnu.ac.kr.

■ ACKNOWLEDGMENT

This work was supported by the National Research Foundation (NRF) funded by the MEST (2010−0027665). We thank Y. S. Bae for his help with experiments.

■ REFERENCES

(1) Bavykin, D. V.; Friedrich, J. M.; Walsh, F. C. *Adv. Mater.* **2006**, *18*, 2807–2824.
(2) Jiang, C.; Wei, M.; Qi, Z.; Kubo, T.; Honma, I.; Haoshen, Z. *J. Power sources* **2007**, *166*, 239–243.
(3) Zhang, H.; Li, G. R.; An, L. P.; Yan, T. Y.; Gao, X. P.; Zhu, H. Y. *J. Phys. Chem. C* **2007**, *111*, 6143–6148.
(4) Cui, Y.; Liu, L.; Li, B.; Zhou, X.; Xu, N. *J. Phys. Chem. C* **2010**, *114*, 2434–2439.
(5) Iida, M.; Sasaki, T.; Watanabe, M. *Chem. Mater.* **1998**, *10*, 3780–3782.
(6) Wang, J.; Zhou, Y.; Hu, Y.; O'Hayre, R.; Shao, Z. *J. Phys. Chem. C* **2011**, *115*, 2529–2536.
(7) Kubiak, P.; Geserick, J.; Husing, N.; Mehrens, M. W. *J. Power Sources* **2008**, *175*, 510–516.
(8) Wang, Z.; Liu, S.; Chen, G.; Xia, D. *Electrochem. Solid-State Lett.* **2007**, *10*, A77–A80.
(9) Soler-Illia, G. J. de A. A.; Louis, A.; Sanchez, C. *Chem. Mater.* **2002**, *14*, 750–759.
(10) Cao, F.-F.; Wu, X.-L.; Guo, Y.-G.; Wan, L.-J. *J. Phys. Chem. C* **2010**, *114*, 10308–10313.
(11) Lafont, U.; Simonin, L; Gaberscek, M.; Kelder, E.M. *J. Power Sources* **2007**, *174*, 1104–1108.
(12) Wang, J.; Bai, Y.; Wu, M.; Yin, J.; Zhang, W. F. *J. Power sources* **2009**, *191*, 614–618.
(13) Das, S. K.; Pate, M.; Bhattacharyya, A. J. *ACS Appl. Mater. Interfaces* **2010**, *2*, 2091–2099.
(14) Dambournet, D.; Belharouak, I.; Amine, K. *Chem. Mater.* **2010**, *22*, 1173–1179.
(15) Kavan, L.; Rathousky, J.; Gratzel, M.; Shklover, V.; Zukal, A. *J. Phys. Chem. B* **2000**, *104*, 12012–12020.
(16) Armstrong, A.R.; Armstrong, G.; Canales, J.; Bruce, P.G. *Angew. Chem., Int. Ed.* **2004**, *43*, 2286–2288.
(17) Zhang, Y.; Wu, L.; Zeng, Q.; Zhi, J. *J. Phys. Chem. C* **2008**, *112*, 16457–16462.
(18) Choi, M.-G.; Lee, Y.-G.; Song, S.-W.; Kim, K. M. *Electrochim. Acta* **2010**, *55*, 5975–5983.
(19) Xu, K. *Chem. Rev.* **2004**, *104*, 4303–4418.
(20) Kim, J. H.; Song, S.-W.; Hoang, H. V.; Doh, C.-H.; Kim, D.-W. *Bull. Korean Chem. Soc.* **2011**, *32*, 105–108.
(21) Song, S.-W.; Baek, S.-W. *Electrochem. Solid-State Lett.* **2009**, *12*, A23–A27.
(22) Nguyen, C.C.; Song, S.-W. *Electrochem. Commun.* **2010**, *12*, 1593–1595.
(23) Galiński, M.; Lewandowski, A.; Stępniak, I. *Electrochim. Acta* **2006**, *51*, 5567–5580.
(24) Lux, S. F.; Schmuck, M.; Appetecchi, G. B.; Passerini, S.; Winter, M.; Balducci, A. *J. Power Sources* **2009**, *192*, 606–611.
(25) Mun, J.; Jung, Y. S.; Yim, T.; Lee, H. Y.; Kim, H.-J.; Kim, Y. G.; Oh, S. M. *J. Power Sources* **2009**, *194*, 1068–1074.
(26) Nguyen, C.C.; Kim, D.-W.; Song, S.-W. *J. Electrochem. Sci. Technol.* **2011**, *2*, 8–13.
(27) Muhlebach, J.; Muller, K.; Schwarzenbach, G. *Inorg. Chem.* **1970**, *9*, 2381–2390.
(28) Schwarzenbach, D. *Inorg. Chem.* **1970**, *9*, 2391–2397.
(29) Tomita, K.; Petrykin, V.; Kobayashi, M.; Shiro, M.; Yoshimura, M.; Kakihana, M. *Angew. Chem. Int. Ed.* **2006**, *45*, 2378–2381.
(30) Gong, X. Q.; Selloni, A.; Batzill, M.; Diebold, U. *Nat. Mater.* **2006**, *5*, 665–670.
(31) Diebold, U. *Surf. Sci. Rep.* **2003**, *48*, 53–229.
(32) Lowell, S.; Shields, J. E.; Thomas, M. A.; Thomas, M. In *Characterization of Porous Solids and Powders: Surface Area, Pore Size and Density*; Kluwer Academic: Dordrecht, The Netherlands, 2004.
(33) Saravanan, K.; Ananthanarayanan, K.; Balaya, P. *Energy Environ. Sci.* **2010**, *3*, 939–948.
(34) Ren, Y.; Hardwick, L. J.; Bruce, P. G. *Angew. Chem., Int. Ed.* **2010**, *14*, 2570–2574.
(35) Krol, R. V. D.; Goossens, A.; Meulenkamp, E. A. *J. Electrochem. Soc.* **1999**, *146*, 3150–3154.
(36) Wagemaker, M.; Kearley, G. J.; van Well, A. A.; Mutka, H.; Mulder, F. M. *J. Am. Chem. Soc.* **2003**, *125*, 840–848.
(37) Aurbach, D.; Zaban, A. *J. Electroanal. Chem.* **1995**, *393*, 43–53.
(38) Aurbach, D.; Markovsky, B.; Shechter, A.; Ein-Eli, Y. *J. Electrochem. Soc.* **1996**, *143*, 3809–3820.
(39) Ong, T. S.; Yang, H. *J. Electrochem. Soc.* **2002**, *149*, A1–A8.
(40) Zhang, S. S.; Xu, K.; Jow, T. R. *Electrochim. Acta* **2006**, *51*, 1636–1640.
(41) Pfanzelt, M.; Kubiak, P.; Fleischhammer, M.; Wohlfahrt-Mehrens, M. *J. Power Sources* **2011**, *196*, 6815–6821.